Earth, Planets and Space

FULL PAPER

Open Access

Geomagnetic conjugacy of plasma bubbles extending to mid-latitudes during a geomagnetic storm on March 1, 2013

Takuya Sori[1*] , Yuichi Otsuka[1], Atsuki Shinbori[1], Michi Nishioka[2] and Septi Perwitasari[2]

Abstract

This study, for the first time, reports the geomagnetically conjugate structure of a plasma bubble extending to the mid-latitudes and the asymmetrical structure of the decay of the plasma bubble during a geomagnetic storm. We investigated the temporal and spatial variations of plasma bubbles in the Asian sector during a geomagnetic storm on March 1, 2013, using Global Navigation Satellite System-total electron content data with high spatiotemporal resolutions. The first important point of our data analysis results is that the plasma bubble extended from the equator to the mid-latitudes with geomagnetic conjugacy along the magnetic field lines. The total electron content data showed that the plasma bubbles appeared in the equatorial regions near 150° E after sunset during the main phase of the geomagnetic storm. From ionosonde data over both Japan and Australia, they suggest that a large eastward electric field existed in the Asian sector. Finally, the plasma bubbles extended up to the mid-latitudes (~ 43° geomagnetic latitude) in both hemispheres, maintaining geomagnetic conjugacy. The second point is that the mid-latitude plasma bubble disappeared 1–2 h earlier in the northern hemisphere than in the southern hemisphere at close to midnight. In the northern hemisphere, the ionospheric virtual height decreased near midnight, followed by a rapid decrease in the total electron content and a rapid increase in the ionospheric virtual height. These results imply that the mid-latitude plasma bubble disappeared as the background plasma density decreased after midnight due to the recombination resulting from the descent of the F layer. Therefore, we can conclude that mid-latitude plasma bubbles can be asymmetric between the northern and southern hemispheres because of the rapid decay of plasma bubbles in one of the hemispheres.
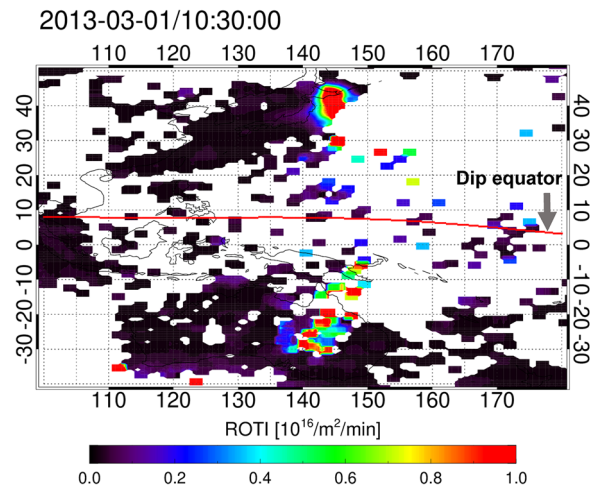
Keywords: Ionosphere, Geomagnetic storm, Rate of total electron content index, Plasma bubbles, Mid-latitudes, Geomagnetic conjugacy

*Correspondence: sori.takuya@isee.nagoya-u.ac.jp
[1] Institute for Space-Earth Environmental Research (ISEE), Nagoya University, Nagoya, Japan
Full list of author information is available at the end of the article

Sori *et al. Earth, Planets and Space*   (2022) 74:120

Page 2 of 16

Graphical Abstract

2013-03-01/10:30:00

ROTI [10^{16}/m^2/min]

Main text

Introduction

After sunset, a plasma density depletion (plasma bubble) often occurs at the bottom of the F-region over the equator. Plasma bubbles exhibit plasma density irregularities (Booker and Wells 1938; Woodman and La Hoz 1976; McClure et al. 1977; Tsunoda 1980a; Abdu et al. 1983; Kelley et al. 2002; Fukao et al. 2004; Saito et al. 2008; Tulasi Ram et al. 2017). It is widely accepted that plasma bubbles are caused by the Rayleigh–Taylor instability (RTI) mechanism (Farley et al. 1970; Sultan 1996; Kelley 2009), and an eastward electric field is one of the most important factors for increasing the growth rate of the RTI. In the equatorial region, an enhancement of the eastward electric field (a pre-reversal enhancement, PRE) occurs after sunset and generates upward $\mathbf{E} \times \mathbf{B}$ plasma drifts (Kelley 2009). The PRE contributes to plasma bubble generation mainly during geomagnetically quiet days (e.g., Basu et al. 1996; Lee et al. 2005; Abadi et al. 2015; Smith et al. 2015).

During geomagnetic storms under the southward interplanetary magnetic field (IMF) condition, the convection electric field in the high-latitude ionosphere intensifies. This enhanced electric field instantaneously penetrates from the high-latitude ionosphere to the low-latitude equatorial ionospheres (Kikuchi et al. 2008, 2010), and this is referred to as the penetration of the convection electric field. The polarity of this penetration is eastward in the dayside and dusk ionospheres and westward in the nightside ionosphere (Nishida 1968; Kikuchi et al. 1996, 2008, 2010; Fejer et al. 2008; Kikuchi and Hashimoto 2016; Nilam et al.

2020). Since the penetration of the convection electric field can be superposed on the PRE in the dusk sector, causing larger upward plasma drifts (Fejer et al. 1999), it also increases the growth rate of the RTI associated with plasma bubble generation. Previous studies have reported that plasma bubbles have been generated by the superposed eastward electric field after sunset during the main phase of geomagnetic storms using global positioning system (GPS) or global navigation satellite system (GNSS) receivers (Ma and Maruyama 2006; Cherniak and Zakharenkova 2016; Aa et al. 2018; Li et al. 2018; Zakharenkova and Cherniak 2020; Sori et al. 2021). On the other hand, in the recovery phases of geomagnetic storms the creation of plasma bubbles after sunset is often suppressed by penetration of electric fields. These would be caused by over-shielding and/or a disturbance dynamo (e.g., Rajesh et al. 2017; Zakharenkova et al. 2019; Sori et al. 2021). Since the polarity of these electric fields is westward in the dayside and dusk ionospheres and eastward in the nightside ionosphere (Abdu 2012; Kikuchi and Hashimoto 2016; Navarro et al. 2019), they weaken eastward PRE at sunset terminator.

Plasma bubbles are formed along magnetic field lines (Tsunoda 1980b) and extend to higher altitudes and latitudes; therefore, they have been observed in both hemispheres at geomagnetic conjugate points (Otsuka et al. 2002a; Shiokawa et al. 2004, 2015; Martinis and Mendillo 2007; de Paula et al. 2010; Park et al. 2016). Otsuka et al. (2002a) and Shiokawa et al. (2004) found that airglow depletions associated with plasma bubbles were observed with geomagnetic conjugacy at Sata, Japan [24° N;

Sori *et al. Earth, Planets and Space* (2022) 74:120

Page 3 of 16

geomagnetic latitude (GMLAT)] and Darwin, Australia (22° S; GMLAT). Martinis and Mendillo (2007) and Park et al. (2016) investigated a temporal variation of plasma density depletions using all-sky imagers at Arecibo, Puerto Rico (28° N; GMLAT), and El Leoncito, Argentina (18° S; GMLAT), which is relatively close to the Arecibo conjugate point. de Paula et al. (2010) also reported that plasma density irregularities related to plasma bubbles were observed at geomagnetically conjugate points in Boa Vista (11° N; GMLAT) and Campo Grande (11° S; GMLAT), Brazil, using GPS receivers. Although storm-time plasma bubbles often extend to mid-latitudes because of the superposed eastward electric field (Ma and Maruyama 2006; Cherniak and Zakharenkova 2016; Aa et al. 2018; Li et al. 2018; Zakharenkova and Cherniak 2020), conjugate observation of plasma bubbles extending to mid-latitudes has not yet been performed. Previous studies have reported that storm-time plasma bubbles extend to mid-latitudes in the northern hemisphere, whereas no similar observations have been reported in the southern hemisphere. This is probably due to the lower number of GNSS receivers in the southern compared to northern hemisphere or the decay of these plasma bubbles in this region.

In the present study, we found for the first time that plasma bubbles initiated in the Asian sector extended to the mid-latitudes in both the northern and southern hemispheres with geomagnetic conjugacy during a geomagnetic storm on March 1, 2013. After midnight, the mid-latitude plasma density irregularities related to plasma bubbles in the northern hemisphere disappeared earlier than those in the southern hemisphere.

Datasets and processing
To investigate temporal variations of the IMF, solar wind dynamic pressure, solar wind velocity, and SYM-H index during the geomagnetic storm on March 1, 2013, we used high-resolution OMNI (HRO) data provided by the National Aeronautics and Space Administration's (NASA's) Coordinated Data Analysis Web (CDAWeb) (https://cdaweb.gsfc.nasa.gov/), and the SYM-H index (Iyemori 1990; Iyemori and Rao 1996) provided by the World Data Center for Geomagnetism, Kyoto University (https://wdc.kugi.kyoto-u.ac.jp).

We collected a considerable number of receiver-independent exchange (RINEX) files from many regional GNSS receiver networks from post-1988. In March 2013, there were more than 7000 GNSS receivers worldwide. The RINEX files were provided by several data providers listed in the GNSS-TEC database (http://stdb2.isee.nagoya-u.ac.jp/GPS/GPS-TEC/gnss_provider_list.html).

The total electron content (TEC) was obtained from the dual-frequency carrier phase and pseudorange data

in the RINEX files. In this study, we used the vertical TEC, the rate of TEC index (ROTI) (Pi et al. 1997), and the detrended TEC. The vertical TEC was derived by removing inter-frequency biases using the method reported by Otsuka et al. (2002b). ROTI was defined as the standard deviation of the rate of the TEC (ROT) for 5 min, with ROT signifying the time change rate of the TEC for 30 s in units of TECU/min. The detrended TEC was calculated by subtracting the 1-h running average data of the measured TEC from the measured value (Saito et al. 1998). In this analysis, we used vertical TEC, detrended TEC, and ROTI data with a satellite zenith angle of less than 75°. These TEC data were gridded to $0.25° \times 0.25°$ with latitude and longitude in geographic coordinates, assuming a thin-shell ionosphere at a height of 300 km (Sori et al. 2019; Shinbori et al. 2020).

The ionosonde data from Wakkanai (45.16° N, 141.75° E) and Townsville (19.63° S, 146.85° E), provided by the National Institute of Information and Communications (https://wdc.nict.go.jp/IONO/index_E.html) and Space Weather Services (https://www.sws.bom.gov.au/World_Data_Centre/2/2), respectively, were used to investigate the temporal variations in ionospheric virtual height (h'F) at mid-latitudes in the northern and southern hemispheres during the geomagnetic storm and the geomagnetically quiet days in March 2013. The quiet and disturbed days were determined from the list provided by the GFZ German Research Center for Geosciences (https://www.gfz-potsdam.de/en/kp-index/).
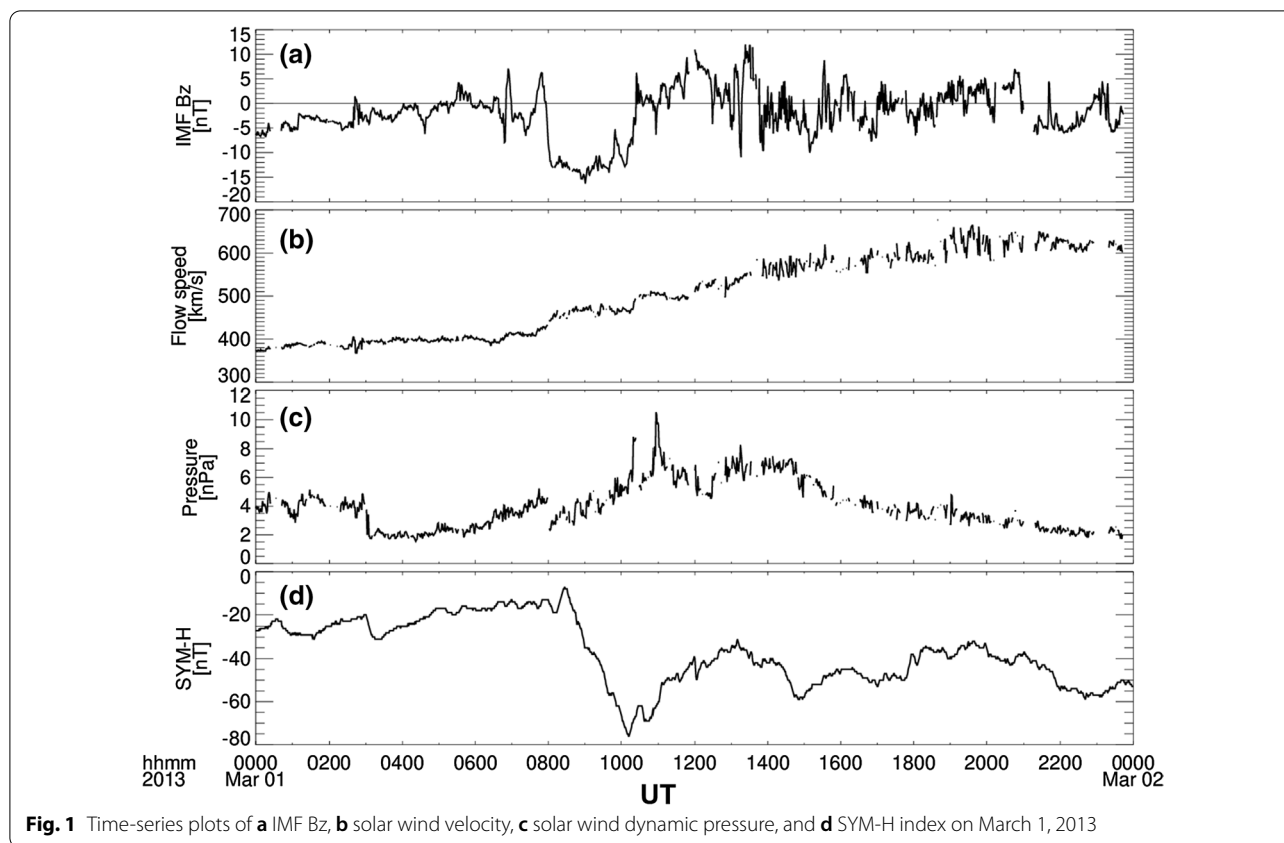
We used O^+ and H^+ densities observed by the Defense Meteorological Satellite Program (DMSP) F-18 satellite to identify the existence of plasma density depletions. The data were provided by the National Oceanic and Atmospheric Administration (https://satdat.ngdc.noaa.gov/dmsp/).

The International Geomagnetic Reference Field (IGRF)-13 model (Alken et al. 2021) was used to obtain the geomagnetic conjugate points in the Asian sector. We also used the altitude-adjusted corrected geomagnetic (AACGM) model to convert the geographic to geomagnetic coordinates at an altitude of 300 km (Shepherd 2014). Data analysis software (Tanaka et al. 2013) developed by the Inter-University Upper Atmosphere Global Observation NETwork project (Hayashi et al. 2013) and Space Physics Environment Data Analysis Software (Angelopoulos et al. 2019) were used for the analysis.

Results
Geomagnetic conditions
Figure 1 is an overview of the geomagnetic conditions during the geomagnetic storm of March 1, 2013. The IMF Bz in Fig. 1a is directed southward from 07:56–10:24 UT. After the northward turning of the IMF, the IMF Bz

Fig. 1 Time-series plots of **a** IMF Bz, **b** solar wind velocity, **c** solar wind dynamic pressure, and **d** SYM-H index on March 1, 2013

showed multiple fluctuations in southward and northward directions. The solar wind speed increased significantly from 410 km/s at 07:40 UT to 660 km/s at 19:37 UT. The solar wind dynamic pressure was also enhanced near 08:00 UT, and reached the maximum of 10.5 nPa at 10:56 UT. The SYM-H index decreased from -7 nT at 08:27 UT to a minimum value of -76 nT at 10:12 UT.

Geomagnetic conjugacy of plasma bubble

Figure 2 shows two-dimensional (2D) maps of ROTI in the Asian sector from 09:00–10:45 UT on March 1, 2013, which reveal spatiotemporal evolutions of ROTI enhancement associated with plasma bubbles in both northern and southern hemispheres. The red curve in each panel indicates the dip equator at a height of 300 km. The dip equator is located at a horizontal latitude of the magnetic field obtained from the IGRF-13 model. The ROTI enhancement appeared in the evening sector near 150° E at 09:15 UT during the main phase of the geomagnetic storm (Fig. 2b). It formed symmetrically at magnetically low latitudes in both northern and southern hemispheres with respect to the dip equator. The enhanced ROTI region extended to higher latitudes in both hemispheres with time, as shown in Fig. 2c–h. The

ROTI enhancement reached approximately 45° N and -30° N at 10:45 UT (Fig. 2h).

We show a 2D map of ROTI in the Asian sector at 09:50 UT and an orbit path of the DMSP F-18 satellite near 09:50 UT on March 1, 2013 to clarify the existence of plasma density depletions in Fig. 3. The curve in the 2D map indicates O^+ density along the DMSP satellite path at a height of $\sim$850 km around 09:50 UT. Enhanced ROTI regions extending from the equator to mid-latitudes near 150° E were observed between -20° and 30° N as shown in Fig. 3a. During this time, the DMSP satellite passed through the northern part of this region and detected ion density depletions, corresponding to the enhanced ROTI regions. Figure 3b and c shows temporal variations of O^+ and H^+ densities observed by the DMSP F-18 satellite during 09:40–10:00 UT on 1 March. O^+ and H^+ densities showed a sudden decrease near the geographic equator during 09:46–09:50 UT and in the low and mid-latitudes during 09:51–09:56 UT.

Figure 4 shows 2D maps of ROTI over Japan and Australia from 09:40–10:50 UT on March 1, 2013. A 2D map of ROTI over Japan is shown on the left of each panel. To clarify geomagnetic conjugacy of the ROTI enhancements, ROTI over Australia is projected onto the magnetically conjugate points in the northern hemisphere
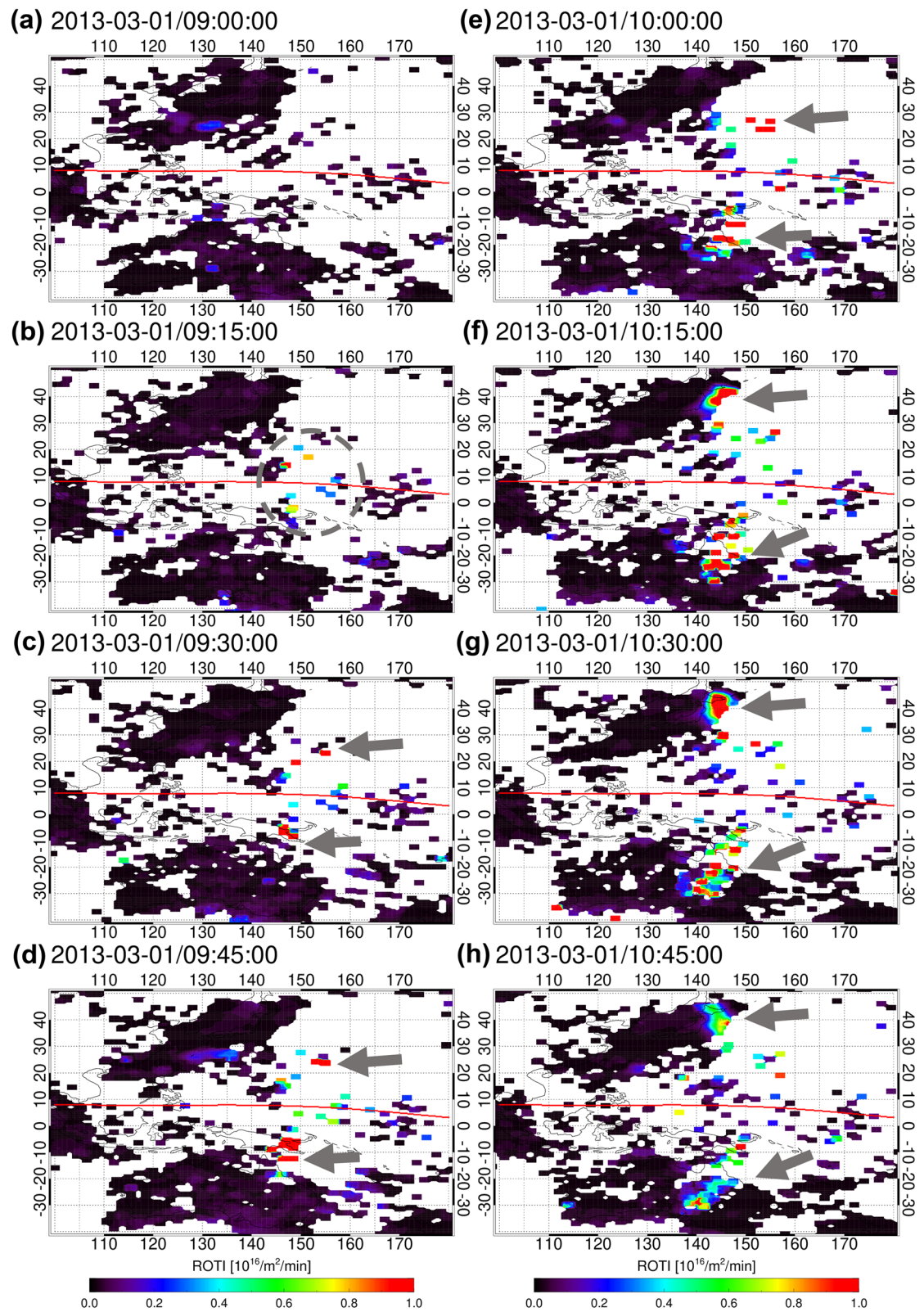
Sori *et al. Earth, Planets and Space*   (2022) 74:120

Page 5 of 16

Fig. 2 a–f Two-dimensional maps of ROTI near Japan and Australia showing 15-min intervals from 09:00–10:45 UT on March 1, 2013. The red curve in each panel indicates the dip equator at a height of 300 km calculated with the IGRF-13 model. The dotted circle and arrows in panels **b–h** show the location of ROTI enhancements, respectively. The color code indicates the ROTI value within a range of 0.0 to 1.0 TECU/min
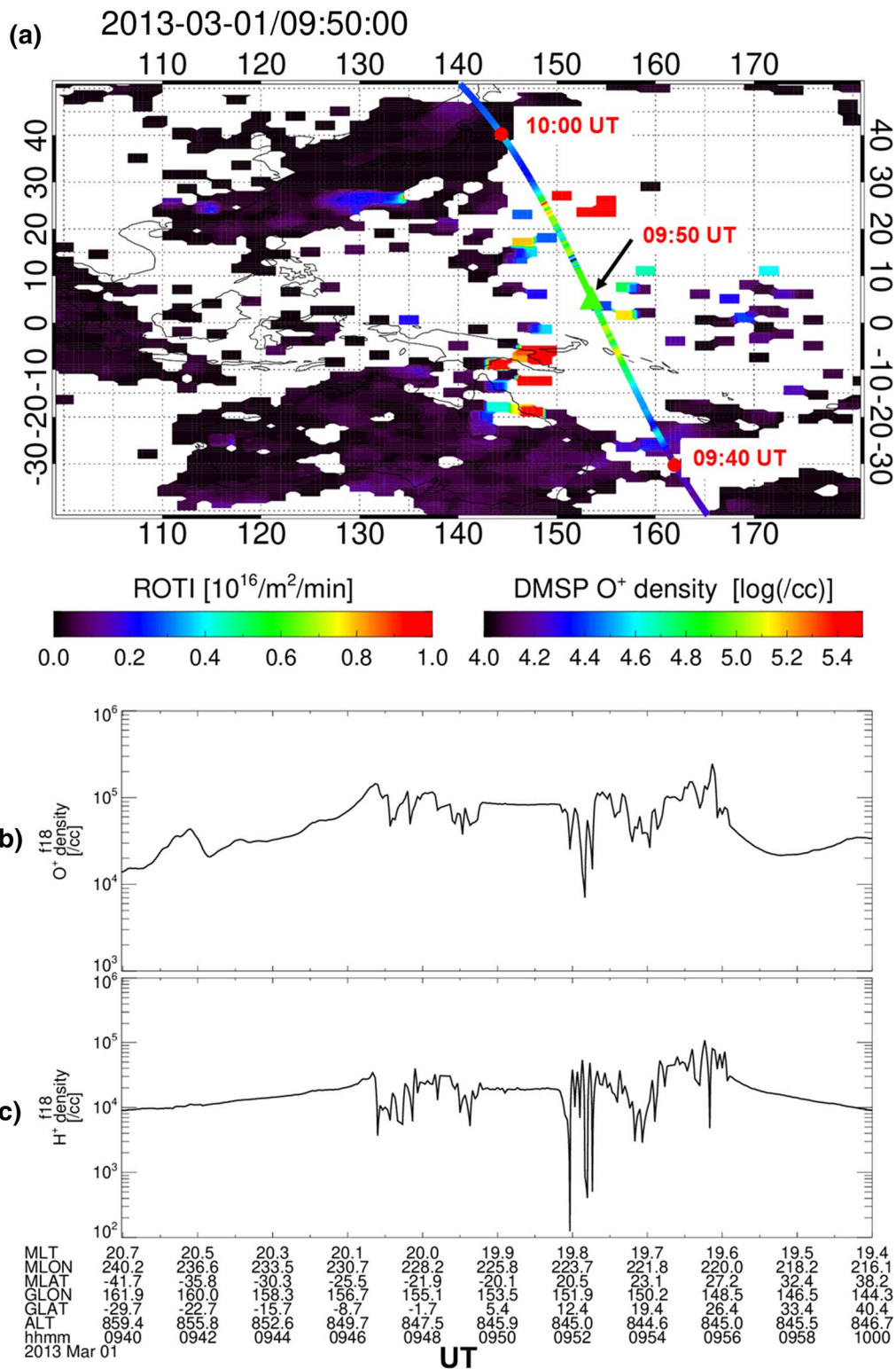
Fig. 3 Panel **a** Two-dimensional maps of ROTI and O$^+$ density observed by the DMSP F-18 satellite near Japan and Australia at 09:50 UT on March 1, 2013. The curve indicates O$^+$ density along the DMSP satellite path around 09:50 UT. The left and right color codes indicate ROTI and O$^+$ density values observed by the DMSP satellite, respectively. The triangle and red circles on the path indicate the DMSP satellite locations at 09:50 UT and 09:40 and 10:00 UT, respectively. Panels **b** and **c** Time-series plots of O$^+$ and H$^+$ densities observed by the DMSP F-18 satellite during 09:40–10:00 UT on 1 March 2013

Sori *et al. Earth, Planets and Space*   (2022) 74:120
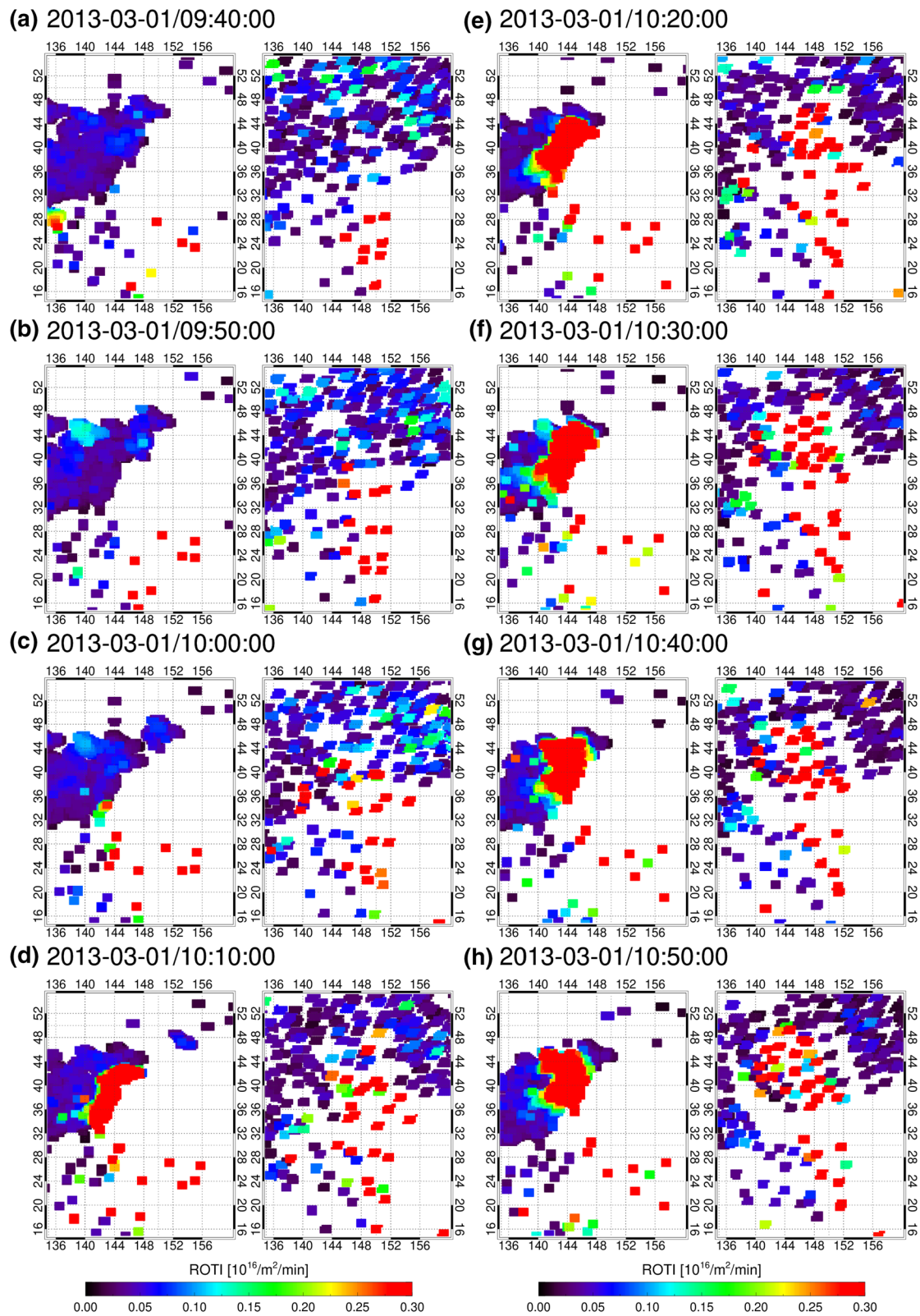
Page 7 of 16

Fig. 4 Two-dimensional maps of ROTI near Japan and Australia showing 10-min intervals from 09:40 to 10:50 UT on March 1, 2013. In each panel, ROTI values over Japan are shown on the left while those over Australia mapped onto the northern hemisphere along the magnetic field lines using the IGRF-13 model are shown on the right. The color code indicates the ROTI value within a range of 0.0 to 0.3 TECU/min

Sori *et al. Earth, Planets and Space*   (2022) 74:120

Page 8 of 16

along the magnetic field lines using the IGRF-13 model. The projected ROTI map is shown on the right in Fig. 4. In Fig. 4a, the enhanced ROTI regions which could represent the plasma density irregularity within plasma bubbles appeared around Japan at 146°–154° E and 16°–28° N, and near Australia at 146°–152° E and 16°–28° N. Both enhanced ROTI regions extended to the higher latitudes with time as shown in Fig. 4b–e. After 10:30 UT, the ROTI enhancement over Japan reached 46° N, which is a poleward edge of the GNSS coverage, while that projected from Australia reached a maximum of 48° N (Fig. 4f–h). The geographic latitude of 48° N in the Japanese sector was ~43° N in GMLAT, which was calculated from the AACGM model. The apex altitude at (48° N, 145° E in geographic coordinates) was approximately 5000 km over the dip equator using the IGRF-13 model.

North–south asymmetry during the decay phase of mid-latitude plasma bubble

Figure 5 shows 2D maps of ROTI over Japan and Australia mapped onto the northern hemisphere from 12:00–17:00 UT on March 1, 2013 at a 1-h interval. The format is the same as that in Fig. 4. The enhanced ROTI region over Japan can be observed at 140°–152° E and 34°–48° N at 12:00 UT, and decayed with time. After that, it disappeared near 15:00 UT as shown in Fig. 5d–f. In contrast, the enhanced ROTI region over Australia mapped onto the northern hemisphere can be seen at 140°–154° E and 36°–48° N from 12:00–17:00 UT although the amplitude of ROTI value became small with time.

Figure 6 shows 2D maps of detrended TEC over Japan and Australia mapped onto the northern hemisphere from 12:00–17:00 UT on March 1, 2013. The detrended TEC variation corresponding to the enhanced ROTI regions can be observed over Japan at 140°–152° E and 34°–48° N at 12:00 UT (Fig. 6a). Existence of plasma bubble in the detrended TEC was not clearly visible after 16:00 UT (Fig. 6e andf), whereas the detrended TEC variation over Australia can be seen at mid-latitudes from 12:00–17:00 UT where the enhanced ROTI region existed.

Furthermore, we show temporal variations in the ROTI and detrended TEC in the northern (45° N) and southern (geomagnetic conjugate points to 45° N) hemispheres as a function of geographic longitude in Fig. 7. Mid-latitude ROTI enhancements and TEC perturbations continuously existed between 140° and 145° E in the northern hemisphere until 15:00–16:00 UT (Fig. 7b and d), while those in the southern hemisphere endured between 140° and 150° E until 17:00 UT (Fig. 7c and e).

Ionospheric background conditions

Figure 8 shows the temporal and spatial variations of vertical TEC as ionospheric conditions during the geomagnetic storm and geomagnetically quiet day. Figure 8a shows the temporal variation of the SYM-H index during the geomagnetic storm, and duplicates Fig. 1d. Figure 8b is a time-series plot of the vertical TEC between 15° and 55° N at 142° E geographic coordinates on March 1. We calculated the geomagnetic conjugate points in the southern hemisphere for this location using the IGRF-13 model, and show a time-series plot of the vertical TEC in the conjugate points in Fig. 8c. Before the onset of the geomagnetic storm at 08:27 UT, the latitudinal distributions of the vertical TEC in the two hemispheres were approximately symmetric, although the vertical TEC was slightly larger in the southern hemisphere. After the onset of the geomagnetic storm, the temporal variation in the vertical TEC in each hemisphere was quite different. The vertical TEC at mid-latitudes higher than 30° in the northern hemisphere was approximately half that of the conjugate points in the southern hemisphere. The TEC at 30–50° N in the northern hemisphere decreased to less than 5 TECU after 14:30 UT.

To clarify the difference in temporal variations of the vertical TEC during the geomagnetic storm to that of the geomagnetically quietest day in March 2013 (March 8), the temporal variation of vertical TEC can be observed near Wakkanai (45.0° N, 142.0° E) and at the geomagnetically conjugate point to Wakkanai (-28.4° N, 138.0° E) in Fig. 8d and e, respectively. The black (red) curve in each panel indicates the vertical TEC during the geomagnetic storm (geomagnetically quiet day) at each location. As shown in Fig. 8d, the vertical TEC near Wakkanai in the northern hemisphere from 09:30 to 11:00 UT and 14:00 to 24:00 UT was less during the geomagnetic storm than during the geomagnetically quiet day and reached less than 5 TECU at approximately 10:00 UT and from 14:30–20:30 UT, respectively. In contrast, the vertical TEC near the geomagnetic conjugate point of Wakkanai in the southern hemisphere from 10:00 to 16:00 UT was greater during the geomagnetic storm than that of the geomagnetically quiet day, as shown in Fig. 8e. After that, the vertical TEC near the geomagnetic conjugate point of Wakkanai from 16:00 to 24:00 UT was comparable to that during the geomagnetically quiet day. Figure 8f and g shows temporal variations in h'F at Wakkanai in Japan and Townsville in Australia, respectively, during the geomagnetic storm and geomagnetically quiet day. The h'F at both Wakkanai and Townsville had significant movement to higher altitudes around 09:00 UT simultaneously
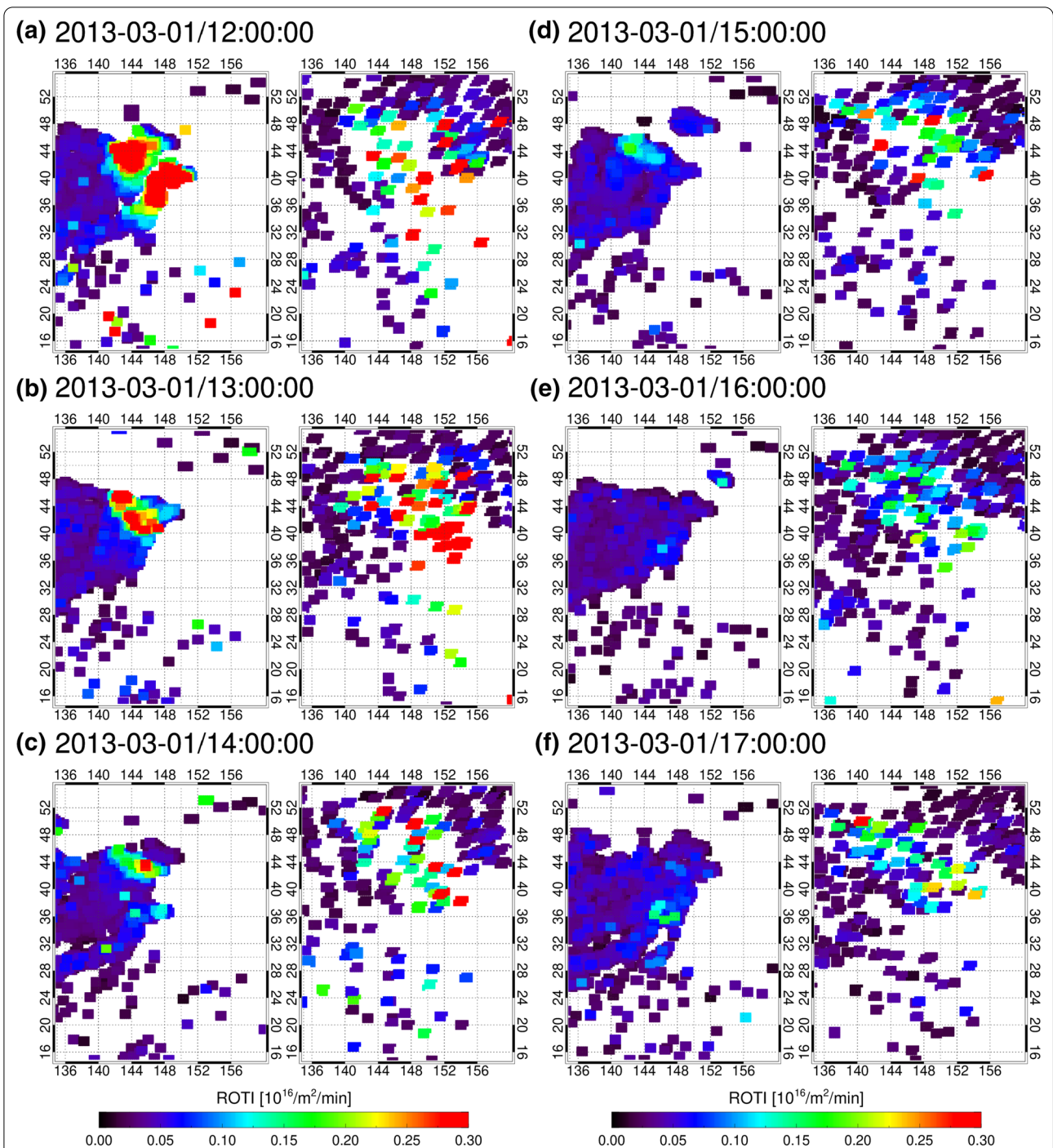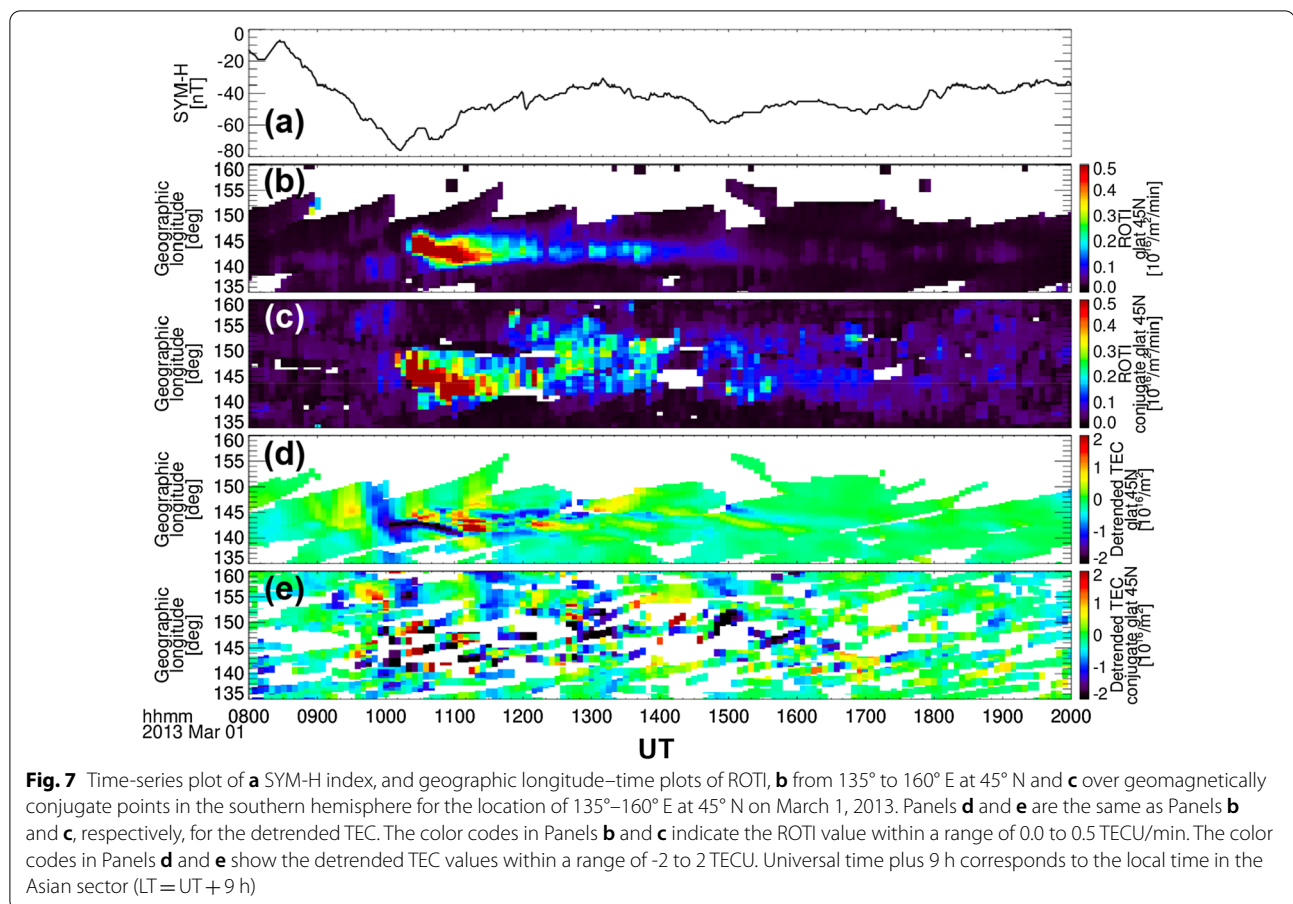
(a) 2013-03-01/12:00:00

(b) 2013-03-01/13:00:00

(c) 2013-03-01/14:00:00

(d) 2013-03-01/15:00:00

(e) 2013-03-01/16:00:00

(f) 2013-03-01/17:00:00

ROTI [10^{16}/m^2/min]

0.00   0.05   0.10   0.15   0.20   0.25   0.30

Fig. 5 Two-dimensional maps of ROTI near Japan and Australia at 1-h intervals from 12:00–17:00 UT on March 1, 2013. In each panel, ROTI values over Japan are shown on the left while those over Australia mapped onto the northern hemisphere along the magnetic field lines using the IGRF-13 model are shown on the right. The color code indicates the ROTI value within a range of 0.0 to 0.3 TECU/min

Fig. 6 Same as Fig. 5, but for the detrended TEC. The color code indicates the detrended TEC value within a range of − 2 to 2 TECU
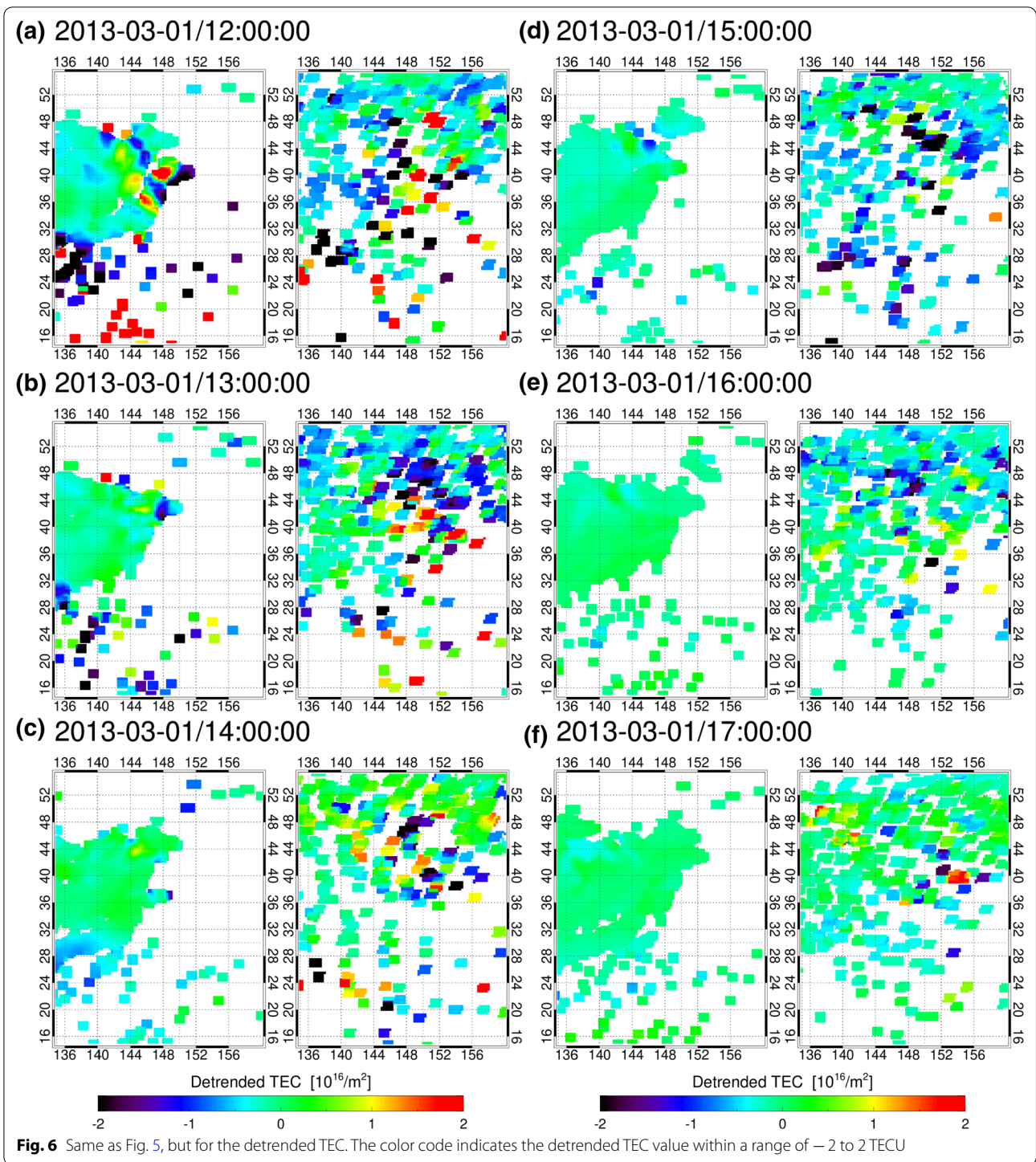
during the southward IMF, and the peak altitude of h'F was higher than that during the geomagnetically quiet day. The h'F at Wakkanai descended rapidly by 60 km near 13:00 UT and reached an altitude of 220 km, which

was lower than that during the geomagnetically quiet day. It then ascended rapidly at approximately 15:30 UT when the TEC quickly decreased, and descended to the quiet level at approximately 20:30 UT. The storm-time
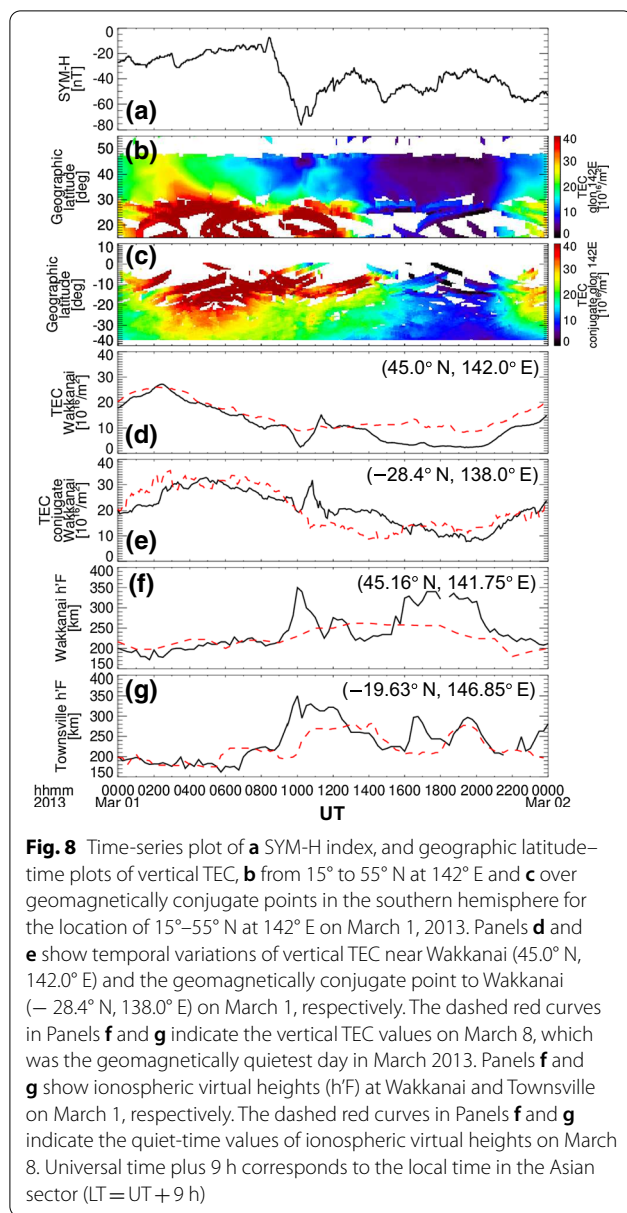
Fig. 7 Time-series plot of **a** SYM-H index, and geographic longitude–time plots of ROTI, **b** from 135° to 160° E at 45° N and **c** over geomagnetically conjugate points in the southern hemisphere for the location of 135°–160° E at 45° N on March 1, 2013. Panels **d** and **e** are the same as Panels **b** and **c**, respectively, for the detrended TEC. The color codes in Panels **b** and **c** indicate the ROTI value within a range of 0.0 to 0.5 TECU/min. The color codes in Panels **d** and **e** show the detrended TEC values within a range of -2 to 2 TECU. Universal time plus 9 h corresponds to the local time in the Asian sector (LT = UT + 9 h)

h'F in Townsville after 13:00 UT was comparable to that during the geomagnetically quiet day, except for the time interval between 16:00 and 18:00 UT.

Discussion

We observed magnetically conjugate structures of plasma bubbles extending to mid-latitudes in both northern and southern hemispheres connected by the geomagnetic field line during a magnetic storm on March 1, 2013. First, we discuss the origin of the plasma bubble generation during the geomagnetic storm. As shown in Fig. 2b, ROTI enhancement in the equatorial region associated with the plasma bubble was observed in the Asian sector near dusk after the IMF Bz turned southward. At this time, the h'F in both hemispheres showed a higher altitude than that during the geomagnetically quiet day. This suggests that the eastward electric field penetrated from high latitudes to the equator in both hemispheres during this period due to the enhanced convection electric field (Kikuchi et al., 2008, 2010). The PRE indicating a strong eastward electric field normally occurs in the equatorial region at close to the sunset terminator (Fejer et al. 1991). In addition, Fejer et al. (2008) reported

that the penetration of the convection electric field was directed eastward on the dayside equator and that the eastward electric field showed a peak value near dusk. Therefore, it is suggested that the enhanced eastward electric fields caused by the PRE and penetration of the convection electric field over the equator were responsible for plasma bubble generation through the RTI during the geomagnetic storm. Previous studies have reported that plasma bubbles can extend to higher latitudes in the dusk sector during geomagnetic storms than under geomagnetically quiet conditions (e.g., Ma and Maruyama 2006; Cherniak and Zakharenkova 2016; Aa et al. 2018; Li et al. 2018; Zakharenkova and Cherniak 2020). Those authors concluded that enhanced eastward electric fields caused by the PRE and the penetration of the convection electric field caused an extension of plasma bubbles to higher latitudes during geomagnetic storms than those in geomagnetically quiet conditions. In this study, the plasma bubbles that appeared over the equatorial region extended to mid-latitudes of ~ 43° (GMLAT) during the geomagnetic storm, as seen in the 2D ROTI maps. It is inferred that the plasma bubbles extending to the mid-latitudes during the geomagnetic storm were caused by

Sori *et al. Earth, Planets and Space* (2022) 74:120

Page 12 of 16

Fig. 8 Time-series plot of **a** SYM-H index, and geographic latitude–time plots of vertical TEC, **b** from 15° to 55° N at 142° E and **c** over geomagnetically conjugate points in the southern hemisphere for the location of 15°–55° N at 142° E on March 1, 2013. Panels **d** and **e** show temporal variations of vertical TEC near Wakkanai (45.0° N, 142.0° E) and the geomagnetically conjugate point to Wakkanai (− 28.4° N, 138.0° E) on March 1, respectively. The dashed red curves in Panels **f** and **g** indicate the vertical TEC values on March 8, which was the geomagnetically quietest day in March 2013. Panels **f** and **g** show ionospheric virtual heights (h'F) at Wakkanai and Townsville on March 1, respectively. The dashed red curves in Panels **f** and **g** indicate the quiet-time values of ionospheric virtual heights on March 8. Universal time plus 9 h corresponds to the local time in the Asian sector (LT = UT + 9 h)

the superposed eastward electric fields of the PRE and penetration of the convection electric field.

In previous studies, plasma bubbles extending to mid-latitudes during geomagnetic storms were observed only in the northern hemisphere. This is because the southern hemisphere had less GNSS receivers compared to the northern hemisphere, or because the plasma bubbles had decayed in the southern hemisphere. For example, Zakharenkova and Cherniak (2020) investigated plasma bubbles in the American sector during a geomagnetic storm on May 27 and 28, 2017 using GNSS data. The plasma bubbles were observed within ± 15°–20° GMLAT, whereas they extended to the mid-latitudes in only the

northern hemisphere subsequently. Those authors concluded that the latitudinal extension was not in altitudinal and latitudinal directions along magnetic field lines, but a horizontal transportation of the plasma bubbles due to storm-time enhanced westward plasma streams, such as the sub-auroral polarization streams (SAPS). Some studies have investigated the temporal and spatial variations of plasma bubbles generated in the American or Asian sector during a geomagnetic storm on September 7 and 8, 2017 (e.g., Aa et al. 2018; Li et al. 2018; Zakharenkova and Cherniak 2020). However, those studies focused on the spatiotemporal variations and cause of plasma bubble generation only in the northern hemisphere and did not discuss the geomagnetic conjugacy of the plasma bubbles at mid-latitudes during the geomagnetic storm in detail. Some reports state that under magnetically quiet conditions, plasma bubbles were observed at geomagnetic conjugate points in both the northern and southern hemispheres, and that the plasma bubbles have magnetically conjugated structures (Otsuka et al. 2002a; Shiokawa et al. 2004, 2015; Martinis and Mendillo 2007; de Paula et al. 2010). These conjugate observations were restricted to narrow, low-latitude regions, and the plasma bubbles were confined to magnetically low mid-latitudes. In this study, using global GNSS data, for the first time, we found that plasma bubbles that expanded to mid-latitudes (∼ 43° GMLAT) during the geomagnetic storm have geomagnetically conjugate structures (Fig. 4). The apex altitude of these bubbles was ∼ 5000 km. Our results suggest that the plasma bubbles maintain their conjugate structures in both hemispheres, connected by geomagnetic field lines during their growth to mid-latitudes. The eastward electric fields generated in the plasma bubbles could play an important role in extending plasma density depletion to higher latitudes. An electric field with a scale larger than 100 km can be transmitted along the magnetic field line without substantial attenuation (Farley 1960).

North–south asymmetry was observed during the decay phase of the plasma bubbles, and we discuss the cause of this asymmetry, which occurred during the geomagnetic storm. Results in Figs. 5, 6, 7 indicate that plasma density irregularities and perturbations associated with plasma bubbles vanished earlier in the northern than the southern hemisphere. As shown in Fig. 8, the vertical TEC in the northern hemisphere decreased rapidly at approximately 15:00 UT, when the plasma bubbles disappeared in this region. In contrast, the vertical TEC in the southern hemisphere gradually decreased between 14:00 and 20:00 UT. Before the rapid reduction in the vertical TEC in the northern hemisphere, the F layer at Wakkanai quickly declined by approximately 60 km around 13:00 UT, and the F layer altitude on this night

Sori *et al. Earth, Planets and Space*   (2022) 74:120

Page 13 of 16

was lower than that on the magnetically quiet night. The rapid TEC decrease could be caused by the quick descent of the F layer to lower altitudes, where the recombination rate was high. Due to the increase in the recombination rate at lower altitudes, the F-region plasma density significantly decreased, and the virtual height observed by ionosondes appeared to increase (e.g., Shiokawa et al. 2002; Otsuka et al. 2003). The rapid increase in h'F at Wakkanai at 15:30 UT could represent the disappearance of the F-region plasma. Therefore, it was inferred that the plasma density irregularities and fluctuations due to plasma bubbles disappear when the F-region plasma density is reduced.

Generally, plasma density structures decay because of diffusion perpendicular to geomagnetic field lines (Kelley 2009). The realistic explanation of the observations perhaps involves a complicated interplay between asymmetric background conditions and perpendicular diffusion rates in both hemispheres as well as ambipolar diffusion along the field-lines in between. This should/will be modeled in more detail in the future. Smaller-scale structures disappeared earlier (Basu et al. 1978). Under geomagnetically quiet conditions, the plasma density depletion caused by plasma bubbles, which have structures with a zonal scale size of approximately 100 km, is maintained throughout the night. However, in this case, the plasma density depletion in the northern hemisphere disappeared when the F-region plasma was reduced. Plasma density structures, including small-scale irregularities due to plasma bubbles, could disappear due to the rapid recombination, as well as background plasma. In the southern hemisphere, the TEC decrease was slower than that in the northern hemisphere during the nighttime, indicating that the F-region plasma density was maintained and the plasma density structures and irregularities survived longer than those in the northern hemisphere.

We also discuss a cause of north–south asymmetry of ionospheric background conditions during the geomagnetic storm. A positive (negative) ionospheric storm which is characterized by an increase (decrease) of plasma density in the low- and mid-latitudes can be caused by the equatorward (poleward) thermospheric neutral wind during geomagnetic storms (e.g., Lin et al. 2005; Balan et al. 2009, 2010; Yue et al. 2016). In the present analysis, the vertical TEC in the northern (southern) hemisphere during the recovery phase of the geomagnetic storm was equal to or smaller (larger) than that during the geomagnetically quiet day as shown in Fig. 8. Furthermore, the F layer in the h'F at Wakkanai quickly declined by approximately 60 km around 13:00 UT and rapidly increased at 15:30 UT due to the increase in the recombination rate at lower altitudes. Considering the

above observational results, it can be inferred that a trans-equatorial northward thermospheric wind leads to the north–south asymmetry of vertical TEC.

Conclusions

Using high temporal and spatial resolution GNSS-TEC data, we found that during a geomagnetic storm on March 1, 2013, equatorial plasma bubbles extended to the mid-latitudes in both northern and southern hemispheres with geomagnetic conjugacy, and that the mid-latitude plasma bubbles disappeared earlier in the northern than in the southern hemispheres.

ROTI enhancements appeared over the magnetic equator in the evening sector during the main phase of the geomagnetic storm. They extended to the mid-latitudes in both hemispheres with geomagnetic conjugacy. From the observational results of ionosonde (h'F), they suggest that the eastward electric field can be enhanced in the dusk sector due to the penetration of the convection electric field and cause plasma bubbles to extend from the low to mid-latitudes during the geomagnetic storm. Therefore, these observational facts show that equatorial plasma bubbles extended to mid-latitudes in both hemispheres, maintaining geomagnetic conjugacy.

ROTI enhancements and TEC fluctuations (detrended TEC) in the mid-latitudes disappeared in the northern hemisphere after the rapid increase in h'F and decrease in mid-latitude vertical TEC in the northern hemisphere. These results suggest that the plasma density depletions and irregularities related to plasma bubbles vanished as the background ionospheric plasma density significantly decreased. Therefore, we can conclude that mid-latitude plasma bubbles can be asymmetric between the northern and southern hemispheres because of the rapid decay of plasma bubbles in one of the hemispheres.

Sori *et al. Earth, Planets and Space*   (2022) 74:120

Page 14 of 16

Availability of data and materials
Solar wind and IMF data were provided by NASA's CDAWeb (https://cdaweb.gsfc.nasa.gov/). We used the SYM-H index provided by the World Data Center (WDC) for Geomagnetism, Kyoto University (http://wdc.kugi.kyoto-u.ac.jp/index.html, World Data Center for Geomagnetism, Kyoto et al. 2022). The RINEX data used for GNSS-TEC processing were provided by 50 data providers listed on the webpage of the GNSS-TEC database (http://stdb2.isee.nagoya-u.ac.jp/GPS/GPS-TEC/gnss_provider_list.html). The main contributors were UNAVCO (https://www.unavco.org/data/gps-gnss/gps-gnss.html), CDDIS (https://cddis.nasa.gov/archive/gnss/data/daily/, Noll 2010), CHAIN (http://chain.physics.unb.ca/chain/pages/data_download, Jayachandran et al. 2009), PNGA (http://www.geodesy.cwu.edu, Pacific Northwest Geodetic Array (PANGA), 1996), IBGE (http://geoftp.ibge.gov.br/informacoes_sobre_posicionamento_geodesico/rbmc/dados/), SOPAC (http://garner.ucsd.edu/), GEONET (https://www.gsi.go.jp/ENGLISH/geonet_english.html), GNNZ (https://www.geonet.org.nz/data/types/geodetic), RENAG (https://doi.org/10.15778/resif.rg, RESIF 2017), SONEL (https://www.sonel.org/-GPS-.html), LINZ (https://www.geodesy.linz.govt.nz/positionz/?page=text), INGV (http://ring.gm.ingv.it/, INGV RING Working Group 2016), SWSBM (https://www.sws.bom.gov.au/World_Data_Centre/1/1), AFREF (http://afrefdata.org/), TLALOCNET (http://tlalocnet.udg.mx/tlalocnetgsac/), NCEDC (https://ncedc.org/bard.overview.html, NCEDC 2014), EUREF (https://www.epncb.oma.be/, Bruyninx et al. 2019), RAMSAC (https://www.ign.gob.ar/NuestrasActividades/Geodesia/Ramsac/DescargaRinex, Pinon et al. 2018), and BIGF (http://www.bigf.ac.uk/data_access.html). The ionosonde data over Wakkanai and Townsville were provided by the National Institute of Information and Communications (https://wdc.nict.go.jp/IONO/index_E.html) and Space Weather Services (https://www.sws.bom.gov.au/World_Data_Centre/2/2), respectively. The DMSP satellite data were provided by the National Oceanic and Atmospheric Administration (https://satdat.ngdc.noaa.gov/dmsp/).

Declarations

Author details
[1]Institute for Space-Earth Environmental Research (ISEE), Nagoya University, Nagoya, Japan. [2]National Institute of Information and Communications Technology (NICT), Tokyo, Japan.

References
Aa E, Huang W, Liu S, Ridley A, Zou S, Shi L et al (2018) Midlatitude plasma bubbles over China and adjacent areas during a magnetic storm on 8 September 2017. Space Weather 16:321–331. https://doi.org/10.1002/2017SW001776

Abadi P, Otsuka Y, Tsugawa T (2015) Effects of pre-reversal enhancement of E B drift on the latitudinal extension of plasma bubble in Southeast Asia. Earth Planets Space 67:74. https://doi.org/10.1186/s40623-015-0246-7

Abdu MA (2012) Equatorial spread F/plasma bubble irregularities under storm time disturbance electric fields. J Atmos Solar Terr Phys 75–76:44–56. https://doi.org/10.1016/j.jastp.2011.04.024

Abdu MA, de Medeiros RT, Sobral JHA, Bittencourt JA (1983) Spread F plasma bubble vertical rise velocities determined from spaced ionosonde observations. J Geophys Res 88:9197–9204

Alken P, Thebault E, Beggan CD, Amit H, Aubert J, Baerenzung J et al (2021) International geomagnetic reference field: the thirteenth generation. Earth Planets Space 73:49. https://doi.org/10.1186/s40623-020-01288-x

Angelopoulos V, Cruce P, Drozdov A, Grimes EW, Hatzigeorgiu N, King DA et al (2019) The space physics environment data analysis system (SPEDAS). Space Sci Rev 215(1):9. https://doi.org/10.1007/s11214-018-0576-4

Balan N, Alleyne H, Otsuka Y, Vijaya LD, Fejer BG, McCrea I (2009) Relative effects of electric field and neutral wind on positive ionospheric storms. Earth Planets Space 61(4):439–445

Balan N, Shiokawa K, Otsuka Y, Kikuchi T, Vijaya Lekshmi D, Kawamura S et al (2010) A physical mechanism of positive ionospheric storms at low and mid latitudes through observations and modeling. J Geophys Res 115:A02304. https://doi.org/10.1029/2009JA014515

Basu S, Basu Su, Aarons J, McClure JP, Cousins MD (1978) On the coexistence of kilometer- and meter-scale irregularities in the nighttime equatorial F region. J Geophys Res 83:4219–4226

Basu S et al (1996) Scintillations, plasma drifts, and neutral winds in the equatorial ionosphere after sunset. J Geophys Res 101(A12):26795–26809. https://doi.org/10.1029/96JA00760

Booker HG, Wells HW (1938) Scattering of radio waves in the F region of ionosphere. Terr Mag Atmos Electr 43:249

Bruyninx C, Legrand J, Fabian A, Pottiaux E (2019) GNSS metadata and data validation in the EUREF Permanent Network. GPS Solut 23:106. https://doi.org/10.1007/s10291-019-0880-9

Cherniak I, Zakharenkova I (2016) First observations of super plasma bubbles in Europe. Geophys Res Lett 43:11137–11145. https://doi.org/10.1002/2016GL071421

de Paula ER, Muella MTAH, Sobral JHA, Abdu MA, Batista IS, Beach TL, Groves KM (2010) Magnetic conjugate point observations of kilometer and hundred-meter scale irregularities and zonal drifts. J Geophys Res 115:A08307. https://doi.org/10.1029/2010JA015383

Farley DT (1960) A theory of electrostatic fields in the ionosphere at nonpolar geomagnetic latitudes. J Geophys Res 65(3):869–877. https://doi.org/10.1029/JZ065i003p00869

Farley DT, Balsey BB, Woodman RF, McClure JP (1970) Equatorial spread F: implications of VHF radar observations. J Geophys Res 75(34):7199–7216. https://doi.org/10.1029/JA075i034p07199

Fejer BG, de Paula ER, Gonzáles SA, Woodman RF (1991) Average vertical and zonal F region plasma drifts over Jicamarca. J Geophys Res 96(A8):13901–13906. https://doi.org/10.1029/91JA01171

Fejer BG, Scherliess L, de Paula ER (1999) Effects of the vertical plasma drift velocity on the generation and evolution of equatorial spread F. J Geophys Res 104:19859–19869

Fejer BG, Jensen JW, Su S-Y (2008) Seasonal and longitudinal dependence of equatorial disturbance vertical plasma drifts. Geophys Res Lett 35:L20106. https://doi.org/10.1029/2008GL035584

Fukao S, Ozawa Y, Yokoyama T, Yamamoto M, Tsunoda RT (2004) First observations of the spatial structure of F region 3-m-scale field-aligned irregularities with the Equatorial Atmosphere Radar in Indonesia. J Geophys Res 109:A02304. https://doi.org/10.1029/2003JA010096

Hayashi H, Koyama Y, Hori T, Tanaka Y, Abe S, Shinbori A, et al., Motoba T and IUGONET project team (2013) Inter–university upper atmosphere global observation NETwork (IUGONET). Data Sci J 12: WDS179–WDS184. doi: https://doi.org/10.2481/dsj.WDS 030, 2013

World Data Center for Geomagnetism, Kyoto, Imajo S, Matsuoka A, Toh H, Iyemori T (2022). Mid-latitude geomagnetic indices ASY and SYM (ASY/SYM Indices). Doi:https://doi.org/10.14989/267216.

INGV RING Working Group (2016). Rete Integrata Nazionale GNSS. doi: https://doi.org/10.13127/RING.

Iyemori T (1990) Storm-time magnetospheric currents inferred from mid-latitude geomagnetic field variations. J Geomag Geoelectr 42:1249–1265

Iyemori T, Rao DRK (1996) Decay of the Dst field of geomagnetic disturbance after substorm onset and its implication to storm-substorm relation. Ann Geophys 14:608–618

Jayachandran PT, Langley RB, MacDougall JW, Mushini SC, Pokhotelov D, Hamza AM, Mann IR, Milling DK, Kale ZC, Chadwick R, Kelly T, Danskin DW, Carrano CS (2009) The Canadian high arctic ionospheric network (CHAIN). Radio Sci 44:RS0A0. https://doi.org/10.1029/2008RS004046

Kelley MC (2009) The earth's ionosphere: plasma physics and electrodynamics. International geophysics series, vol 43. Academic Press, San Diego, CA

Kelley MC, Makela J, Ledvina BM, Kinter PM (2002) Observations of equatorial spread-F from Haleakala, Hawaii. Geophys Res Lett 29(20):2003. https://doi.org/10.1029/2002GL015509

Kikuchi T, Hashimoto KK (2016) Transmission of the electric fields to the low latitude ionosphere in the magnetosphere-ionosphere current circuit. Geosci Lett 3(1):1–11. https://doi.org/10.1186/s40562-016-0035-6

Kikuchi T, Lühr H, Kitamura T, Saka O, Schlegel K (1996) Direct penetration of the polar electric field to the equator during a DP2 event as detected by the auroral and equatorial magnetometer chains and the EISCAT radar. J Geophys Res 101(A8):17161–17173

Kikuchi T, Hashimoto KK, Nozaki K (2008) Penetration of magnetospheric electric fields to the equator during a geomagnetic storm. J Geophys Res 113:A06214. https://doi.org/10.1029/2007JA012628

Kikuchi T, Ebihara Y, Hashimoto KK, Kataoka R, Hori T, Watari S, Nishitani N (2010) Penetration of the convection and overshielding electric fields to the equatorial ionosphere during a quasiperiodic DP 2 geomagnetic fluctuation event. J Geophys Res 115:A05209. https://doi.org/10.1029/2008JA013948

Lee C-C, Liu J-Y, Reinisch BW, Chen W-S, Chu F-D (2005) The effect of the pre-reversal drift, the EIA asymmetry, and magnetic activity on the equatorial spread F during solar maximum. Ann Geophys 23:745–751

Li G, Ning B, Wang C, Abdu MA, Otsuka Y, Yamamoto M et al (2018) Storm-enhanced development of postsunset equatorial plasma bubbles around the meridian 120°E/60°W on 7–8 September 2017. J Geophys Res Space Phys 123:7985–7998. https://doi.org/10.1029/2018JA025871

Lin CH, Richmond AD, Heelis RA, Bailey GJ, Lu G, Liu JY et al (2005) Theoretical study of the low- and midlatitude ionospheric electron density enhancement during the October 2003 superstorm: relative importance of the neutral wind and the electric field. J Geophys Res 110:A12312. https://doi.org/10.1029/2005JA011304

Ma G, Maruyama T (2006) A super bubble detected by dense GPS network at east Asian longitudes. Geophys Res Lett 33:L21103. https://doi.org/10.1029/2006GL027512

Martinis C, Mendillo M (2007) Equatorial spread F-related airglow depletions at Arecibo and conjugate observations. J Geophys Res 112:A10310. https://doi.org/10.1029/2007JA012403

McClure JP, Hanson WB, Hoffman JH (1977) Plasma bubbles and irregularities in the equatorial ionosphere. J Geophys Res 82(19):2650–2656. https://doi.org/10.1029/JA082i019p02650

Navarro LA, Fejer BG, Scherliess L (2019) Equatorial disturbance dynamo vertical plasma drifts over Jicamarca: bimonthly and solar cycle dependence. J Geophys Res Space Phys 124:4833–4841. https://doi.org/10.1029/2019JA026729

NCEDC (2014) Northern California Earthquake Data Center. UC Berkeley Seismological Laboratory. Dataset. Doi:https://doi.org/10.7932/NCEDC

Nilam B, Ram ST, Shiokawa K, Balan N, Zhang Q (2020) The solar wind density control on the prompt penetration electric field and equatorial electrojet. J Geophys Res Space Phys 125:e2020JA07869. https://doi.org/10.1029/2020JA027869

Nishida A (1968) Coherence of geomagnetic DP2 fluctuations with interplanetary magnetic variations. J Geophys Res 76:5549

Noll C (2010) The crustal dynamics data information system: a resource to support scientific analysis using space geodesy. Adv Space Res 45(12):1421–1440. https://doi.org/10.1016/j.asr.2010.01.018 (**ISSN 0273-1177**)

Otsuka Y, Shiokawa K, Ogawa T, Wilkinson P (2002a) Geomagnetic conjugate observations of equatorial airglow depletions. Geohys Res Lett. 29(15):43-1-43–4. https://doi.org/10.1029/2002aGL015347

Otsuka Y, Ogawa T, Saito A, Tsugawa T, Fukao S, Miyazaki S (2002b) A new technique for mapping of total electron content using GPS network in Japan. Earth Planets Space 54(1):63–70. https://doi.org/10.1186/BF03352422

Otsuka Y, Kadota T, Shiokawa K, Ogawa T, Kawamura S, Fukao S, Zhang S-R (2003) Optical and radio measurements of a 630-nm airglow enhancement over Japan on 9 September 1999. J Geophys Res 108(A6):1252. https://doi.org/10.1029/2002JA009594

Park J, Martinis CR, Lühr H, Pfaff RF, Kwak Y-S (2016) Hemispheric asymmetry in transition from equatorial plasma bubble to blob as deduced from 630.0 nm airglow observations at low latitudes. J Geophys Res Space Phys 121:881–893. https://doi.org/10.1002/2015JA022175

Pcific Northwest Geodetic Array (PANGA) (1996). GPS/GNSS Network and Geodesy Laboratory: Central Washington University, other/seismic network, International Federation of Digital Seismograph Networks. Doi: https://doi.org/10.7914/SN/PW.

Pi X, Mannucci AJ, Lindqwister UJ, Ho CM (1997) Monitoring of global ionospheric irregularities using the worldwide GPS network. Geophys Res Lett 24(18):2283–2286. https://doi.org/10.1029/97GL02273

Pinon DA, Gomez DD, Smalley R, Cimbaro SR, Lauria EA, Bevis MG (2018) The history, state, and future of the argentine continuous satellite monitoring network and its contributions to geodesy in Latin America. Seismol Res Lett 89(2A):475–482. https://doi.org/10.1785/0220170162

Rajesh PK, Lin CH, Chen CH, Lin JT, Matsuo T, Chou MY, Chen WH, Chang MT, You CF (2017) Equatorial plasma bubble generation/inhibition during 2015 St Patrick's Day Storm. Space Weather 15:1141–1150. https://doi.org/10.1002/2017SW001641

RESIF (2017) RESIF-RENAG French national Geodetic Network. RESIF-Reseau Sismologique et geodesique Francais. https://doi.org/10.15778/resif.rg.

Saito A, Fukao S, Miyazaki S (1998) High resolution mapping of TEC perturbations with the GSI GPS network over Japan. Geophys Res Lett 25:3079–3082

Saito S, Fukao S, Yamamoto M, Otsuka Y, Maruyama T (2008) Decay of 3-m-scale ionospheric irregularities associated with a plasma bubble observed with the Equatorial Atmosphere Radar. J Geophys Res 113:A11318. https://doi.org/10.1029/2008JA013118

Shepherd SG (2014) Altitude-adjusted corrected geomagnetic coordinates: definition and functional approximations. J Geophys Res Space Phys 119:7501–7521. https://doi.org/10.1002/2014JA020264

Shinbori A, Otsuka Y, Sori T, Tsugawa T, Nishioka M (2020) Temporal and spatial variations of total electron content enhancements during a geomagnetic storm on 27 and 28 September 2017. J Geophys Res Space Phys 125:e2019JA026873. https://doi.org/10.1029/2019JA026873

Shiokawa K, Otsuka Y, Ogawa T, Balan N, Igarashi K, Ridley AJ, Knipp DJ, Saito A, Yumoto K (2002) A large-scale traveling ionospheric disturbance during the magnetic storm of 15 September 1999. J Geophys Res 107(A6):1088. https://doi.org/10.1029/2001JA000245

Shiokawa K, Otsuka Y, Ogawa T, Wilkinson P (2004) Time evolution of high-altitude plasma bubbles imaged at geomagnetic conjugate points. Annales De Geophysique 22:3137–3143. https://doi.org/10.5194/angeo-22-3137-2004

Shiokawa K, Otsuka Y, Lynn KJ, Wilkinson P, Tsugawa T (2015) Airglow-imaging observation of plasma bubble disappearance at geomagnetically conjugate points. Earth Planets Space 67:43. https://doi.org/10.1186/s40623-015-0202-6

Smith JM, Rodrigues FS, Fejer BG, Milla MA (2015) Coherent and incoherent scatter radar study of the climatology and day-to-day variability of mean F region vertical drifts and equatorial spread F. J Geophys Res Space Phys 121:1466–1482. https://doi.org/10.1002/2015JA021934

Sori T, Shinbori A, Otsuka Y, Tsugawa T, Nishioka M (2019) Characteristics of GNSS total electron content enhancements over the midlatitudes during a geomagnetic storm on 7 and 8 November 2004. J Geophys Res Space Phys. https://doi.org/10.1029/2019JA026713

Sori T, Shinbori A, Otsuka Y, Tsugawa T, Nishioka M (2021) The occurrence feature of plasma bubbles in the equatorial to midlatitude ionosphere during geomagnetic storms using long-term GNSS-TEC data. J Geophys Res Space Phys 126:e2020JA029010. https://doi.org/10.1029/2020JA029010

Sultan PJ (1996) Linear theory and modeling of the Rayleigh-Taylor instability leading to the occurrence of equatorial spread F. J Geophys Res 101(26):875

Tanaka Y, Shinbori A, Hori T, Koyama Y, Abe S, Umemura N et al (2013) Analysis software for upper atmospheric data developed by the IUGONET project and its application to polar science. Adv Polar Sci 24:231–240. https://doi.org/10.3724/SP.J.1085.2013.00231

Tsunoda RT (1980a) Backscatter measurements of 11-cm equatorial spread-F irregularities. Geophys Res Letts 7(10):848–850

Tsunoda RT (1980b) Magnetic-field-aligned characteristics of plasma bubbles in the nighttime equatorial ionosphere. J Atmos Terr Phys 42:743–752. https://doi.org/10.1016/0021-9169(80)90057-4

Tulasi Ram S, Ajith KK, Yokoyama T, Yamamoto M, Niranjan K (2017) Vertical rise velocity of equatorial plasma bubbles estimated from Equatorial Atmosphere Radar (EAR) observations and HIRB model simulations. J Geophys Res Space Physics 122:6584–6594. https://doi.org/10.1002/2017JA024260

Woodman RF, La Hoz C (1976) Radar observations of F region equatorial irregularities. J Geophys Res 81:5447

Yue X, Wang W, Lei J, Burns A, Zhang Y, Wan W, Liu L, Hu L, Zhao B, Schreiner WS (2016) Long-lasting negative ionospheric storm effects in low and middle latitudes during the recovery phase of the 17 March 2013 geomagnetic storm. J Geophys Res Space Phys 121:9234–9249. https://doi.org/10.1002/2016JA022984

Zakharenkova I, Cherniak I (2020) When plasma streams tie up equatorial plasma irregularities with auroral ones. Space Weather 18:e2019SW002375. https://doi.org/10.1029/2019SW002375

Zakharenkova I, Cherniak I, Krankowski A (2019) Features of Storm-induced ionospheric irregularities from ground-based and spaceborne GPS observations during the2015 St Patrick's Day Storm. J Geophys Res Space Phys. https://doi.org/10.1029/2019JA026782

Publisher's Note